Materialia 14 (2020) 100873

Contents lists available at ScienceDirect

Materialia

journal homepage: www.elsevier.com/locate/mtla

Full Length Article

Thermoelectric power factor of $Ge_{1-x}Sn_x$ thin films

A. Portavoce[a,*], H. Khelidj[a,b], N. Oueldna[a,c], S. Amhil[d], M. Bertoglio[a], D. Mangelinck[a], L. Essaleh[d], K. Hoummada[a]

[a] CNRS/Aix-Marseille University, Faculté des Sciences de Saint-Jérôme case 142, 13397 Marseille, France
[b] L3M, Ecole Nationale Supérieure des Mines et de la Métallurgie, Annaba, Algeria
[c] LASMAR, University of Moulay Ismail, Faculté des Sciences, 11201 Meknes, Morocco
[d] LMCN, Cadi-Ayyad University, Faculty of Sciences and Technology, Department of Applied Physics, Marrakech, Morocco

ARTICLE INFO

Keywords:
Ge1-xsnx
Thin films
Seebeck coefficient
Thermoelectricity

ABSTRACT

The Seebeck coefficients (α) and the power factors of 100 nm-thick $Ge_{1-x}Sn_x$ films grown by magnetron sputtering were studied versus Sn composition ($0.09 \leq x \leq 0.15$) in the 220–330 K temperature range. The films present particularly high Seebeck coefficients at room temperature but as they are undoped, their power factors are too low for room temperature thermoelectric applications due to low electrical conductivity (σ). Nevertheless, as it is possibile to modify both α and σ by adjusting *x*, as well as employ conventional doping techniques, the IV-IV $Ge_{1-x}Sn_x$ semiconductor is shown to be extremely interesting for complementary-metal-oxide-semiconductor-compatible thermoelectric applications.

1. Introduction

Thermoelectric technology refers to heat-to-electricity conversion [1]. In this case, thermoelectric devices exploit a temperature (T) gradient to produce electricity. Their performance is mainly dependent on inherent material properties, such as Seebeck coefficient (α), electrical conductivity (σ), and thermal conductivity (κ) [1]. High-performance thermoelectric devices typically use high-performance thermoelectric materials exhibiting a high power factor $PF = \alpha^2\sigma$ and the highest possible figure of merit $ZT = \alpha^2\sigma T/\kappa$. With the development of mobile microelectronic and communication devices, energy conversion technologies face new challenges, as it is desired to integrate energy harvesting solutions in microelectronic circuits [2]. The goal of integrated energy harvesting devices is to use surrounding energy sources (thermal, mechanical, electromagnetic waves…) to produce electricity that can be used by the mobile device during operation, allowing increased autonomy. This electricity production can be used either to partially charge the device battery (or an integrated supercapacitor), or to execute some operations without soliciting the battery. Thermoelectric devices should be particularly suited to this type of application, since temperature gradients are generally present in microelectronic setups. Furthermore, the required energy supply remains modest, as it does not need to entirely power the device, and mobile devices generally use low-consumption microelectronic circuits. Additionally, thermoelectric modules are solid-state and can be miniaturized. However, microelectronic applications have specific technological constraints: energy harvesting must be performed at temperatures close to room temperature (RT), and in order to be integrated in microelectronic technology, materials as well as their fabrication processes must be compatible with the complementary metal-oxide-semiconductor (CMOS) technology [2]. Moreover, the integrated device should be based on thin films (micro- or nano- structure), and if possible, made of common and non-toxic materials. Accordingly, current thermoelectric materials exhibiting the best thermoelectric properties at RT cannot be used for microelectronic applications. They are not compatible with CMOS technology, and use toxic or rare elements, such as $Bi_xSb_{2-x}Te_3$ (p-type) and $Bi_2Te_{3-x}Se_x$ (n-type) compounds [3,4].

Semiconductors are materials of particular interest for thermoelectric applications, especially due to their doping capabilities. The same semiconductor can be of either p- or n-type controlling dopant nature (control of the carrier type: holes or electrons), with the semiconductor Fermi level and the carrier concentration being adjusted by controlling the dopant concentration, allowing for material ZT engineering [5-8]. Ge(Sn) is a CMOS-compatible IV-IV semiconductor, currently investigated for CMOS optoelectronic applications as well as for Si photonics [9-13]. The $Ge_{1-x}Sn_x$ alloy forms a Ge-Sn binary random solution exhibiting the cubic diamond structure with a lattice parameter a_{GeSn} larger than Ge, following the corrected-Vegard law

$$a_{GeSn} = (1-x)a_{Ge} + x a_{Sn} + bx(1-x) \quad (1)$$

With $a_{Ge} = 0.565$ nm and $a_{Sn} = 0.649$ nm, the Ge and Sn lattice parameters in the diamond structure, respectively, and $b = 0.0041$ nm the bowing coefficient [14-16]. Sn maximum solubility in Ge is only 1.1 at% at 673 K [17] but meta-stable Sn-rich $Ge_{1-x}Sn_x$ thin films can be elab-

* Corresponding author:.
E-mail address: alain.portavoce@im2np.fr (A. Portavoce).

https://doi.org/10.1016/j.mtla.2020.100873
Received 26 May 2020; Accepted 13 August 2020
Available online 19 August 2020
2589-1529/© 2020 Published by Elsevier B.V. on behalf of Acta Materialia Inc.

orated [18]. Interestingly for thermoelectric applications, $Ge_{1-x}Sn_x$ alloys can possess higher carrier mobility [19-21] than Ge alone and lower thermal conductivities [22,23]. Furthermore, Sn composition variations are known to implicate serious modifications of the $Ge_{1-x}Sn_x$ alloy electronic band structure, as the semiconductor electronic band gap (E_g) is indirect for $x \leq 0.1$ and direct for $x \geq 0.1$ [24-26]. Consequently, the $Ge_{1-x}Sn_x$ Seebeck coefficient [27] is expected to be significantly dependent on the alloy Sn composition, allowing for *ZT* engineering with a significant degree of freedom [28,29]. $Ge_{1-x}Sn_x$ films are usually elaborated by molecular beam epitaxy or chemical vapor deposition [15,16,18-21] but magnetron sputtering seems more appropriate for thermoelectric applications [14,30], since it involves a significantly lower production cost, while being CMOS-compatible. This work reports the investigation of the Seebeck coefficient and power factor variations of 100-nm-thick $Ge_{1-x}Sn_x$ films with Sn composition x comprised between 0.09 and 0.15 in the temperature range $220 \leq T \leq 330$ K, for CMOS-compatible RT energy harvesting.

2. Materials and methods

100 nm-thick $Ge_{1-x}Sn_x$ films were deposited in a commercial magnetron sputtering system (base pressure of 10^{-8} Torr) at $T = 673$ K on 1.5×2.5 cm^2 glass substrates. The substrates were subsequently cleansed for 10 min in acetone and alcohol baths in an ultrasonic cleaner, and kept 30 min at 423 K in a baking furnace, before being loaded in the sputtering chamber. Commercial 99.999% Ge-pure and 99.99% Sn-pure targets were co-sputtered using different sputtering powers for Sn in order to get different Sn compositions from $x = 0.0$ to $x = 0.15$. Ge and Sn deposition fluxes were calibrated thanks to ex-situ thickness measurements by X-ray reflectivity. $Ge_{1-x}Sn_x$ film concentrations were systematically determined using X-ray diffraction (XRD), and checked using Rutherford back scattering and atom probe tomography measurements. The microstructure of the films was investigated using XRD in the Bragg-Brentano (θ–2θ) geometry using a Cu K_α source ($\lambda_{K\alpha} = 0.154$ nm). The surface state of the films was checked by atomic force microscopy (AFM). The electrical conductivities of the films were measured with respect to temperature by impedance spectroscopy [31] using an impedance analyzer (HP 4284 A) operated between 20 Hz and 1 MHz, using an alternating signal of 100 mV amplitude. Contacts on the samples were achieved using a silver conductive paste. The temperature variations were controlled using a programmable Thermolyne heater, or using a liquid nitrogen cryostat for the low temperatures. The Seebeck coefficients of the films were measured using a home-made setup [32].

3. Results and discussion

In order to measure the Seebeck coefficient and the electrical conductivity of the 100 nm-thick films without the substrate influence, the $Ge_{1-x}Sn_x$ films were deposited on commercial glass substrates that can exhibit a high surface roughness compared to the surface of regular semiconductor substrates. Fig. 1 a shows an AFM image of the glass substrate before deposition. The substrate exhibits a surface roughness (RMS) $r = 5.13$ nm, which is about one order of magnitude higher than that of a silicon substrate for example, but which is significantly less than the thickness of the films. Furthermore, the surface roughness of the three $Ge_{1-x}Sn_x$ films (Figs. 1a–1d) is found to decrease when the Sn concentration increases: $r = 4.56$, 2.75, and 2.31 nm for $x = 0.09$ (sample #1), 0.13 (sample #2), and 0.15 (sample #3), respectively. The $Ge_{0.91}Sn_{0.9}$ (Fig. 1b) and $Ge_{0.87}Sn_{0.13}$ (Fig. 1c) films show similar average lateral grain size $w \sim 60$ nm, according to AFM observations. However, grains cannot be observed in the AFM images acquired on the surface of the $Ge_{0.85}Sn_{0.15}$ film (Fig. 1d).

Fig. 2a shows the X-ray diffractograms measured in the Bragg-Brentano geometry on the three $Ge_{1-x}Sn_x$ samples as well as on a Ge film

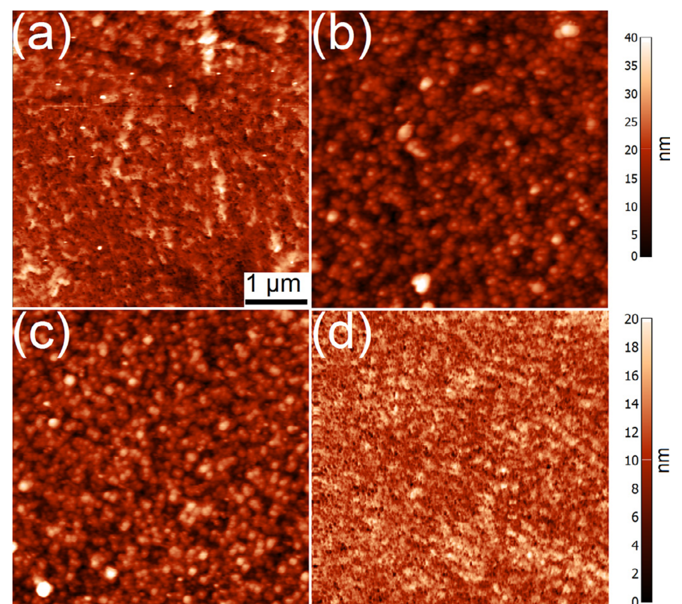

Fig. 1. AFM images obtained on the surface of the glass substrate before growth (a) as well as after the growth of a 100 nm-thick $Ge_{1-x}Sn_x$ film with $x = 0.09$ (b), 0.13 (c), and 0.15 (d).

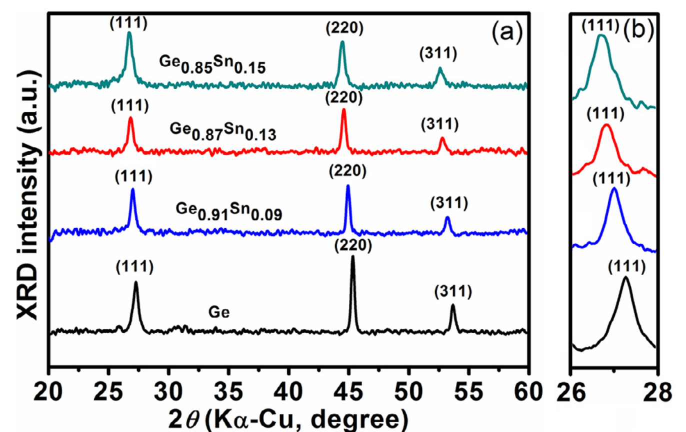

Fig. 2. X-ray diffractograms measured on $Ge_{1-x}Sn_x$ films with $x = 0.0$, 0.09, 0.13, and 0.15.

($x = 0.0$) deposited in the same conditions. The four films are polycrystalline and exhibit the same texture along the normal of the surface: the same four diffraction peaks are observed in each sample, corresponding (from left to right) to the (111), (220), and (311) atomic planes of the diamond structure. Pure-Sn diffraction peaks are not detected. As expected, the shift of $Ge_{1-x}Sn_x$ diffraction peaks towards the lower angles (Fig. 2b) corresponds to $x = 0.09$, 0.13, and 0.15 according to eq. 1.

The diffraction angle of the (111) diffraction peak of each of the three samples is given in Table 1 with the corresponding lattice parameter and Sn composition. The full width at half maximum (FWHM) of the (111) peaks was used to determine the average size d of the $Ge_{1-x}Sn_x$ grains in the direction perpendicular to the film surface using the Scherrer equation [14,27]: $d \sim 30$, 25, and 10 nm for $x = 0.09$, 0.13, and 0.15, respectively. The grains in the $Ge_{1-x}Sn_x$ layers are not columnar and present sizes d in the same range as reported in previous works [14,27]. The comparison between AFM and XRD measurements suggests that the grains are wider than thick, or that the grains located at the surface are bigger than those deeper in the $Ge_{1-x}Sn_x$ films. Furthermore, the grains in the $Ge_{0.85}Sn_{0.15}$ film are significantly smaller than those in the two other films of lower Sn composition according to both AFM and XRD

Table 1
Diffraction angle of the (111) peak (θ), lattice parameter (a), Sn composition (x), and ΔE_α of the three samples #1, #2, and #3. The gap energy (E_g) corresponding to each sample composition according to ref. [55] is also given.

Sample	θ (°)	a (Å)	x	ΔE_α (eV)	E_g (eV) (Indirect)	E_g (eV) (direct)
#1	13.49	5.73	0.09	0.03	0.51	0.53
#2	13.41	5.76	0.13	0.11	0.45	0.42
#3	13.37	5.78	0.15	0.07	0.42	0.37

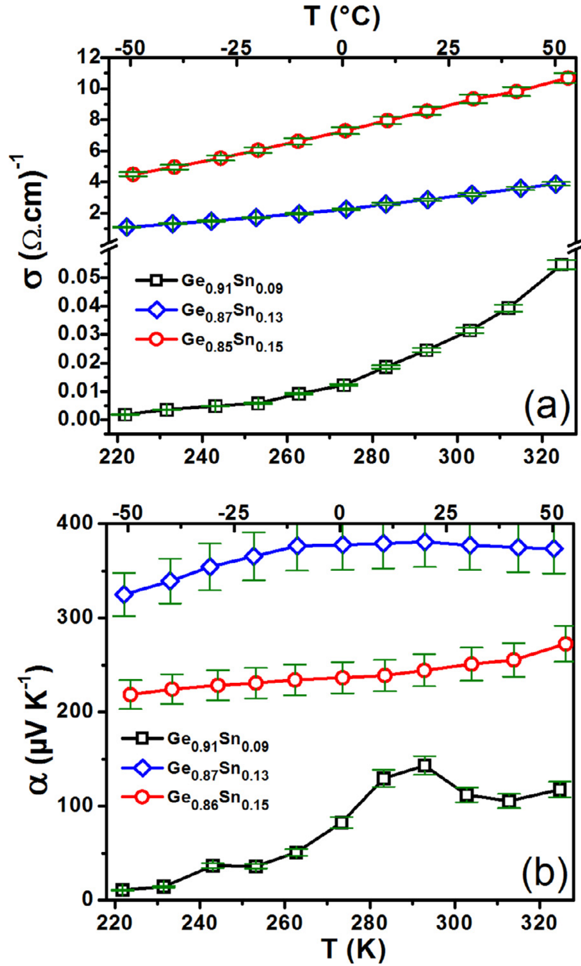

Fig. 3. Electrical conductivity (a) and Seebeck coefficient (b) measured versus temperature on three different 100 nm-thick $Ge_{1-x}Sn_x$ films with $x = 0.09$, 0.13, and 0.15.

measurements. One should note that due to tip effects, the lateral sizes measured by AFM are generally overestimated. Furthermore, the observation of grain boundaries (GBs) by AFM is usually due to the grooving effect [33], as the size of GBs (~ 0.5 nm) is smaller than AFM lateral resolution. Thus, the "grains" observed by AFM could correspond to the aggregation of several grains not separated by the AFM tip.

Fig. 3a presents the electrical conductivity measured on the three $Ge_{1-x}Sn_x$ films versus temperature, in the 220–330 K temperature range. As expected for non-degenerate semiconductor layers, σ increases with temperature and furthermore increases with x, the conductivity of the $Ge_{1-x}Sn_x$ films being higher than the conductivity of intrinsic Ge. For example, $\sigma = 0.029$, 3.08, and 9.05 Ω^{-1} cm^{-1} at 300 K for $x = 0.09$, 0.13, and 0.15, respectively, whereas $\sigma \sim 0.02$ Ω^{-1} cm^{-1} for undoped Ge at the same temperature [34]. One can note that the conductivity of the $Ge_{0.91}Sn_{0.09}$ film is significantly lower (~ two orders of magnitude) than that of the two other $Ge_{0.87}Sn_{0.13}$ and $Ge_{0.86}Sn_{0.15}$ films. This difference may be related to the significant electronic band structure difference between $Ge_{1-x}Sn_x$ alloys of Sn compositions below (indirect band gap) and above (direct band gap) $x = 0.1$ [24,25]. The Seebeck coefficients of the $Ge_{1-x}Sn_x$ films measured in the same temperature range are shown in Fig. 3b. For the three films, α is positive, corresponding to p-type semiconductors. The Seebeck coefficients of the $Ge_{1-x}Sn_x$ films is found to be significantly high around RT, with $\alpha = 120$, 377, and 248 μV K^{-1} at 300 K for $x = 0.09$, 0.13, and 0.15, respectively. In comparison, $\alpha = 190$, 160, 200, and −140 μV K^{-1} for $Bi_{2-x}Sb_xTe_3$ [35], hole-doped SnSe [36], $SnS_{0.91}Se_{0.09}$ [37], and $Mg_2Sn_{0.75}Ge_{0.25}$ [38].

Sn composition variations have a strong impact on the Seebeck coefficient. Variations of α versus temperature are different for each film and are not proportional to x, since at a given temperature $\alpha(x = 0.09) \leq \alpha(x = 0.15) \leq \alpha(x = 0.13)$. The Seebeck coefficient difference between the films is significant despite relatively low composition variations since a difference of about 100 μV K^{-1} separates $\alpha(x = 0.09)$ from $\alpha(x = 0.15)$, as well as $\alpha(x = 0.15)$ from $\alpha(x = 0.13)$. The Seebeck coefficient of a single-valley semiconductor with spherical constant-energy surface can be expressed as [39,40]:

$$\alpha = \pm \frac{\Delta E_\alpha}{qT} \tag{2}$$

q is the elementary charge with the sign "+" for p-type semiconductors or "−" for n-type semiconductors, $\Delta E_\alpha = \varepsilon - E_F$ with E_F the Fermi level energy in the semiconductor, and ε can be considered as the average energy of the charge carriers contributing to the electronic conduction, comprising potential energy (electronic structure) and kinetic energy that is dependent on scattering mechanisms (phonon scattering, ionized impurity scattering…). In the case of non-degenerate doped semiconductors, $|\alpha|$ increases with temperature in the extrinsic temperature range as the Fermi level moves away from the edge of the valence (p-type) or the conduction (n-type) band, and $|\alpha|$ is at a maximum before reaching the mixed conduction temperature range [41]. It was shown that at this maximum $\Delta E_\alpha \sim \frac{1}{2} E_g$ with an error less than 20% (< 3% for Ge) [41], meaning that ε is close to the energy of the valence band (E_V) for p-type semiconductors or to the conduction band for n-type semiconductors (see Fig. 7.12 in ref. [39]). The values of ΔE_α determined from the Seebeck coefficients of the three samples at $T = 300$ K are given in Table 1. Considering in our case that $\Delta E_\alpha \sim |E_V - E_F|$, the hole concentration (p) in the $Ge_{1-x}Sn_x$ films was estimated at $T = 300$ K using the relation:

$$p = N_V exp\left(\frac{-\Delta E_\alpha}{k_B T}\right) \tag{3}$$

N_V is the effective density of states in the valence band of $Ge_{1-x}Sn_x$. Calculations showing that the Ge valence band is not significantly modified by Sn alloying [42,43], the value of N_V was set for all the samples as equal to that of Ge ($N_V = 5 \times 10^{24}$ m^{-3}). The hole concentrations estimated in our samples are compared in Fig. 4 to those measured in relaxed $Ge_{1-x}Sn_x$ layers reported in the literature.

p was also determined for an additional sample grown in the same conditions with $x = 0.06$. Our results are similar to those of the literature, the hole concentrations vary between 5×10^{16} to 5×10^{18} cm^{-3} for $x \leq 0.15$. Experiments [44-46] and ab initio calculations [47] show that holes in undoped $Ge_{1-x}Sn_x$ layers are due to acceptor-like defects formed by the association of substitutional Sn atoms with one or several

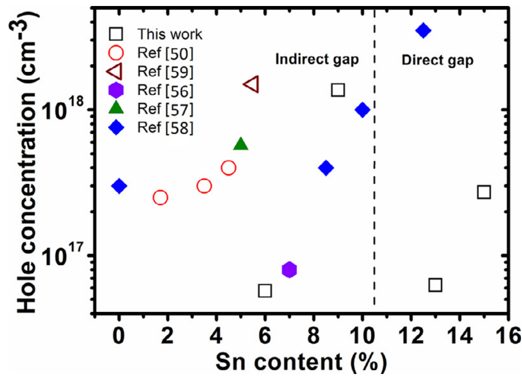

Fig. 4. Hole concentrations in relaxed $Ge_{1-x}Sn_x$ layers. Open symbols correspond to polycrystalline layers, while solid symbols correspond to single crystals. The dashed line shows the indirect-to-direct band gap transition [56–59].

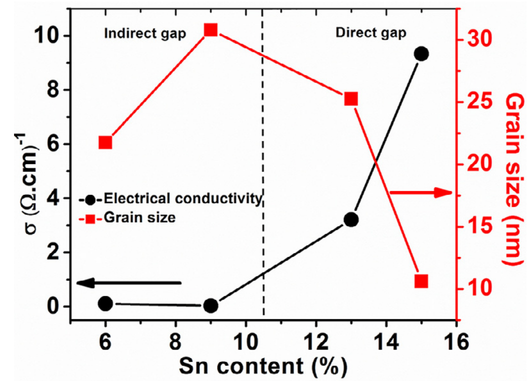

Fig. 5. Electrical conductivity (left axis) and grain size (right axis) measured in the polycrystalline $Ge_{1-x}Sn_x$ layers versus Sn concentration.

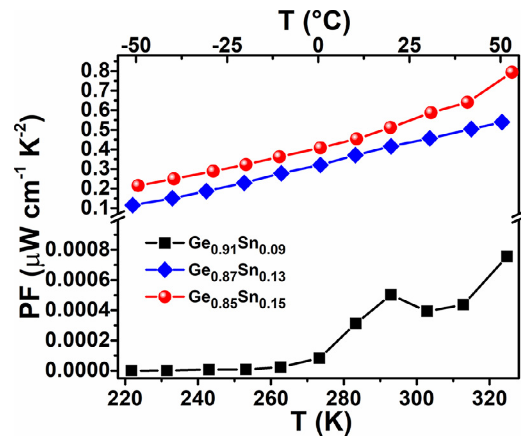

Fig. 6. $Ge_{1-x}Sn_x$ film power factors versus temperature determined from the electrical conductivities and the Seebeck coefficients presented in Fig. 3.

vacancies (*V*) or with dislocations. Due to the lower melting temperature of Sn with respect to Ge, equilibrium vacancy concentration in $Ge_{1-x}Sn_x$ alloys increases with x. Furthermore, layers grown at lower temperatures are expected to contain more vacancies [48,49]. Thus, Sn-rich $Ge_{1-x}Sn_x$ alloys grown at low temperature are expected to exhibit higher hole concentrations. Fig. 4 shows that the hole concentration seems to generally increase with x, but significant variations can be observed for same Sn concentrations depending on authors. Furthermore, these variations cannot be easily attributed to the microstructure (open symbols correspond to polycrystals and solid symbols correspond to monocrystals in Fig. 4) or to the growth temperature (solid hexagon and solid up-triangle correspond to $T \sim 423$ K; and open squares, open left-triangle and solid diamonds correspond to $T \sim 623$ to 723 K in Fig. 4) or to the growth technique (sputtering–open squares; evaporation–open circles; MBE–solid hexagon, solid up-triangle, and open left-triangle; CVD–solid diamonds in Fig. 4). However, in some cases, the hole concentration was shown to decrease if the sample is annealed after growth, especially under hydrogen atmosphere [44], which is in agreement with the mechanisms of point-defect (Sn-*V*) annihilation and/or passivation. In this case, the hole concentration decrease is accompanied by an increase of charge carrier mobility [50], suggesting that acceptor-like Sn-*V* defects have a non-negligible influence on hole scattering.

Sn composition is shown to be an important parameter allowing for the simultaneous modification of α and σ. α is known to depend on the concentration, the effective mass (m^*), and the scattering coefficient (γ) of the charge carriers close to the Fermi level. Eq. (4) corresponds to the case of degenerate semiconductors, but is often used to qualitatively predict the influence of these different parameters on the Seebeck coefficient [3,40].

$$\alpha \propto \frac{m^* T}{q}\left(\frac{\pi}{3p}\right)^{\frac{2}{3}}\left(\frac{3}{2}+\gamma\right) \tag{4}$$

This equation shows that the increase of α through the modification of any of the cited parameters results in a decrease of the electronic conductivity. As expected, the increase of the Seebeck coefficient of the $Ge_{1-x}Sn_x$ films can be associated with a decrease of σ (Eq. (4)): when x decreases from 0.15 to 0.13, α increases from 248 to 377 μV K^{-1} and σ decreases from 9.05 to 3.08 Ω^{-1} cm^{-1} at $T = 300$ K. However, x modification can also remarkably lead to the concomitant increase of α and σ, when x increases from 0.09 to 0.13 or 0.15 (Fig. 3), for example. The simultaneous increase of α and σ has already been observed in nanocrystalline *p*-type Si with high B segregation levels in GBs [40, 51]. This effect was explained by a similar contribution of grains and GBs in charge carrier transport in nanocrystalline structures and the formation of a depletion region around the GBs, allowing for the Fermi level in the GBs to be located in the valence band of the grains but below the energy barrier of the GBs. In our case, Sn is also expected to strongly segregate in extended defects such as GBs, due to the significant difference of melting temperatures between Sn and Ge. Indeed, Sn was observed to segregate in $Ge_{1-x}Sn_x$ threading dislocations for example [52]. Equilibrium segregation in extended defects is known to increase with the impurity bulk concentration. Thus, the amount of Sn segregated in $Ge_{1-x}Sn_x$ GBs is expected to increase with x. Consequently, the effect previously reported in B-doped nanocrystalline Si should have the largest effect on nanocrystalline $Ge_{1-x}Sn_x$ layers exhibiting the smallest grains and the highest Sn concentrations, as observed in this case (Fig. 5).

Furthermore, since the hole concentration is dependent on the formation of Sn-*V* acceptor-like complexes in undoped $Ge_{1-x}Sn_x$, the combined effects of high temperature growth ($T = 673$ K) and *V* annihilation at GBs lead to a particularly low *V* concentration in our films exhibiting nano-grains ($d \leq 30$ nm), leading to a low concentration of Sn-*V* complexes and holes. One can note that when x increases from 0.09 to 0.13 (or 0.15), p decreases from 1.5×10^{18} cm^{-3} to 6.3×10^{16} cm^{-3} (or 2.8×10^{17} cm^{-3}) suggesting a decrease of the Sn-*V* concentration. The decrease of p should favor the increase of α according to Eq. (4), while the decrease of the Sn-*V* concentration should favor the decrease of hole scattering, and thus possibly lead to a simultaneous increase of σ.

Fig. 6 presents the *PF* variations of the $Ge_{1-x}Sn_x$ films versus temperature. The *PF* increases with x despite $\alpha(x = 0.15) \leq \alpha(x = 0.13)$. Due to the large difference in electrical conductivities, the *PF* of the $Ge_{0.91}Sn_{0.09}$ film ($PF = 4.2 \times 10^{-4}$ μW cm^{-1} K^{-2} at 300 K) is much lower than that of the two other films $Ge_{0.87}Sn_{0.13}$ ($PF = 0.44$ μW cm^{-1} K^{-2} at 300 K) and $Ge_{0.86}Sn_{0.15}$ ($PF = 0.56$ μW cm^{-1} K^{-2} at 300 K). Despite significantly high Seebeck coefficients, the *PF* of the films is two orders of magnitude smaller (for $x = 0.13$ and 0.15) than that of current

best materials for RT thermoelectric applications, such as $Bi_xSb_{2-x}Te_3$ [35], hole-doped SnSe [36], $SnS_{0.91}Se_{0.09}$ [37] or $Mg_2Sn_{0.75}Ge_{0.25}$ [38]. The $Ge_{1-x}Sn_x$ *PF* is actually impaired by the low electrical conductivity of the films. For example, for $x = 0.13$ at 300 K $\alpha = 377$ μV K^{-1} but $\sigma = 3.08\ \Omega^{-1}\ cm^{-1}$ leading to $PF = 0.44$ μW $cm^{-1}\ K^{-2}$. Former works have shown that Ge doping with Sn concentrations of about 10^{19} at cm^{-3} ($x = 1 \times 10^{-3}$) is *p*-type and leads to $\sigma \sim 1\ \Omega^{-1}\ cm^{-1}$ with $n \sim 2.2 \times 10^{16}\ cm^{-3}$ [53]. One can note that the hole concentration is in this case three orders of magnitude smaller than the concentration of Sn, which is usually explained considering the formation of the Sn-*V* acceptor-like defects [19,20]. These low-Sn-concentrated layers exhibit *p* and σ of same magnitudes as that of our high-concentrated films. Despite the significant difference in Sn concentrations, our films are still weakly doped [21]. Consequently, doping the $Ge_{1-x}Sn_x$ films with regular dopants such as B can be an interesting way to significantly increase the electrical conductivity of the $Ge_{1-x}Sn_x$ films, likely boosting their power factors. Indeed, three orders of magnitude higher *p*-type and *n*-type doping levels have been demonstrated ($n = 1$ to $5 \times 10^{19}\ cm^{-3}$) in $Ge_{1-x}Sn_x$ using As, P, and B [54].

4. Conclusion

In summary, the power factor of 100 nm-thick polycrystalline $Ge_{1-x}Sn_x$ films with $0.09 \leq x \leq 0.15$ has been determined with the aim of RT CMOS-compatible thermoelectric applications. The $Ge_{1-x}Sn_x$ films are *p*-type and possess particularly high Seebeck coefficients at RT. As expected, Sn composition variations result in significant modifications of α without x being modified proportionally. However, the low electrical conductivity of the layers leads to power factors too low for RT applications. Nevertheless, the Sn composition is shown to be an efficient parameter for modifying both α and σ, sometimes allowing for the concomitant increase of these two factors. Thus, the possibility of adjusting the alloy Sn composition combined with structural and doping modification capabilities offer significant degrees of freedom for $Ge_{1-x}Sn_x$ *PF* and *ZT* engineering. Therefore, $Ge_{1-x}Sn_x$ is a CMOS-compatible semiconductor exhibiting high potential for thermoelectric applications and in particular for those at RT as the electrical conductivity of $Ge_{1-x}Sn_x$ films is potentially increased by three orders of magnitude by conventional doping.

Declaration of Competing Interest

The authors declare that they have no known competing financial interests or personal relationships that could have appeared to influence the work reported in this paper.

CRediT authorship contribution statement

A. Portavoce: Conceptualization, Investigation, Visualization, Supervision, Writing - original draft. **H. Khelidj:** Investigation, Writing - review & editing. **N. Oueldna:** Investigation, Writing - review & editing. **M. Bertoglio:** Resources, Methodology. **D. Mangelinck:** Validation, Writing - review & editing. **L. Essaleh:** Resources, Validation. **K. Hoummada:** Conceptualization, Validation, Supervision, Writing - review & editing.

References

[1] A. Shakouri, Recent Developments in Semiconductor Thermoelectric Physics and Materials, Annu. Rev. Mater. Res 41 (2011) 399–431.
[2] A.P. Perez-Marin, A.F. Lopeandia, L. Abad, P. Ferrando-Villaba, G. Garcia, A.M. Loopez, F.X. Muñoz-Pascual, J. Rodriguez-Viejo, Micropower thermoelectric generator from thin Si membranes, Nano Energy 4 (2014) 73–80.
[3] Y.C. Dou, X.Y. Qin, D. Li, L.L. Li, T.H. Zou, Q.Q. Wang, Enhanced thermopower and thermoelectric performance through energy filtering of carriers in $(Bi_2Te_3)_{0.2}(Sb_2Te_3)_{0.8}$ bulk alloy embedded with amorphous SiO_2 nanoparticles, J. Appl. Phys 114 (2013) 044906.
[4] E. Pozega, S. Ivanov, Z. Stevic, L. Karanovic, R. Tomanec, L. Gomidzelovic, A. Kostov, Identification and characterization of single crystal $Bi_2Te_{3-x}Se_x$ alloy, Trans. Nonferrous Met. Soc. China 25 (2015) 3279–3285.
[5] G. Tan, L.-.D. Zhao, M.G. Kanatzidis, Rationally Designing High-Performance Bulk Thermoelectric Materials, Chem. Rev. 116 (2016) 12123–12149.
[6] J. He, T.M. Tritt, Advances in thermoelectric materials research: Looking back and moving forward, Science 357 (2017) 1369.
[7] C. Gayner, K.K. Kar, Inherent room temperature ferromagnetism and dopant dependent Raman studies of PbSe, $Pb_{1-x}Cu_xSe$, and $Pb_{1-x}Ni_xSe$, J. Appl. Phys 117 (2015) 103906.
[8] C. Gayner, R. Sharma, M.K. Das, K.K. Kar, Boost in room temperature thermoelectric performance of PbSe:Al_x through band modification and low densification, J. Appl. Phys 120 (2016) 155106.
[9] Z. Fang, Q.Y. Chen, C.Z. Zhao, A review of recent progress in lasers on silicon, Opt. Laser Technol 46 (2013) 103–110.
[10] K.P. Homewood, M.A. Lourenço, The rise of the GeSn laser, Nat. Photonics 9 (2015) 78.
[11] Z. Zhou, B. Yin, J. Michel, On-chip light sources for silicon photonics, Light: Sci. Appl 4 (2015) e358.
[12] D. Thomson, A. Zilkie, J.E. Bowers, T. Komljenovic, G.T. Reed, L. Vivien, D. Marris–Morini, E. Cassan, L. Virot, J.-.M. Fédéli, J.-.M. Hartmann, J.H. Schmid, D.-.X. Xu, F. Boeuf, P. O'Brien, G.Z. Mashanovich, M. Nedeljkovic, Roadmap on silicon photonics, J. Opt 18 (2016) 073003.
[13] W. Du, S.-.Q. Yu, Group IV photonics using (Si)GeSn technology toward mid-IR applications, Mid-infrared Optoelectronics 12 (2020) 493–538 https://doi.org/, doi:10.1016/B978-0-08-102709-7.00012-7.
[14] H. Mahmodi, M.R. Hashim, U. Hashim, Formation of nanocrystalline GeSn thin film on Si substrate by sputtering and rapid thermal annealing, Superlattices Microstruct 98 (2016) 235–241.
[15] C. Xu, C.L. Senaratne, R.J. Culbertson, J. Kouvetakis, J. Menéndez, Deviations from Vegard's law in semiconductor thin films measured with X-ray diffraction and Rutherford backscattering: The $Ge_{1-y}Sny$ and $Ge_{1-x}Si_x$ cases, J. Appl. Phys 122 (2017) 125702.
[16] Kil Y.-.H. Kil, S. Kang, T.S. Jeong, K.-.H. Shim, D.-.J. Kim, Y.-.D. Choi, M.J. Kim, T.S. Kim, Effect of Sn Composition in $Ge_{1-x}Sn_x$Layers Grown by Using Rapid Thermal Chemical Vapor Deposition, Journal of the Korean Physical Society 72 (2018) 1063–1068.
[17] A. Gokhale, G.J. Abbaschian, in: Binary Alloy Phase Diagrams, 2, 2nd ed., ASM International, 1990, p. 1964.
[18] M. Oehme, K. Kostecki, M. Schmid, F. Oliveira, E. Kasper, J. Schulze, Epitaxial growth of strained and unstrained GeSn alloys up to 25% Sn, Thin Solid Films 557 (2014) 169–172.
[19] W. Takeuchi, N. Taoka, M. Kurosawa, M. Sakashita, O. Nakatsuka, S. Zaima, High hole mobility tin-doped polycrystalline germanium layers formed on insulating substrates by low-temperature solid-phase crystallization, Appl. Phys. Lett 107 (2015) 022103.
[20] T. Sadoh, Y. Kai, R. Matsumura, K. Moto, M. Miyao, High carrier mobility of Sn–doped polycrystalline-Ge films on insulators by thickness-dependent low-temperature solid-phase crystallization, Appl. Phys. Lett 109 (2016) 232106.
[21] K. Moto, R. Yoshimine, T. Suemasu, K. Toko, Improving carrier mobility of polycrystalline Ge by Sn doping, Sci. Rep 8 (2018) 14832.
[22] N. Uchida, T. Maeda, R.R. Lieten, S. Okajima, Y. Ohishi, R. Takase, M. Ishimaru, J.-.P. Locquet, Carrier and heat transport properties of polycrystalline GeSn films on SiO_2, Appl. Phys. Lett 107 (2015) 232105.
[23] S.N. Khatami, Z. Aksamija, Lattice Thermal Conductivity of the Binary and Ternary Group-IV Alloys Si-Sn, Ge-Sn, and Si-Ge-Sn, Phys. Rev. Appl 6 (2016) 014015.
[24] Guevara H. Pérez Ladrón de, A.G. Rodríguez, H. Navarro-Contreras, M.A. Vidal, Determination of the optical energy gap of $Ge_{1-x}Sn_x$ alloys with 0<x<0.14, Appl. Phys. Lett 84 (2004) 4532–4534.
[25] S. Wirths, R. Geiger, N. von den Driesch, G. Mussler, T. Stoica, S. Mantl, Z. Ikonic, M. Luysberg, S. Chiussi, J.M. Hartmann, H. Sigg, J. Faist, D. Buca, D. Grützmacher, Lasing in direct-bandgap GeSn alloy grown on Si, Nat. Photonics 9 (2015) 88–92.
[26] T.D. Eales, I.P. Marko, S. Schulz, E. O'Halloran, S. Ghetmiri, W. Du, Y. Zhou, S.-.Q. Yu, J. Margetis, J. Tolle, E.P. O'Reilly, S.J. Sweeney, Ge_{1-x} Sn_x alloys: Consequences of band mixing effects for the evolution of the band gap Γ-character with Sn concentration, Sci. Rep. 9 (2019) 14077.
[27] M. Kurosawa, K. Liu, M. Izawa, I. Tsunoda, S. Zaima, Thermoelectric Properties of Ge-Rich GeSn Films Grown on Insulators, ECS Trans 75 (2016) 481.
[28] Y. Pei, H. Wang, G.J. Snyder, Band Engineering of Thermoelectric Materials, Adv. Mater 24 (2012) 6125–6135.
[29] K. C. Gayner an K., K. Kar, Recent advances in thermoelectric materials, Prog. Mat. Sci. 83 (2016) 330–382.
[30] J. Zheng, L. Li, T. Zhou, Y. Zuo, C. Li, B. Cheng, Q. Wang, Growth of Crystalline $Ge_{1-x}Sn_x$ Films on Si (100) by Magnetron Sputtering, ECS Sol. State Lett 3 (2014) P111.
[31] A. Kaushal, S.M. Olhero, B. Singh, uncan P. Fagg, Igor Bdikin, J.M.F. Ferreira, Impedance analysis of $0.5Ba(Zr_{0.2}Ti_{0.8})O_3$–$0.5(Ba_{0.7}Ca_{0.3})TiO_3$ ceramics consolidated from micro-granules, Ceram Int 40 (2014) 10593–10600.
[32] N. Oueldna, A. Portavoce, M. Bertoglio, M. Descoins, A. Kammouni, K. Hoummada, Seebeck coefficient in multiphase thin films, Mater Lett 266 (2020) 127460.
[33] A. Portavoce, E. Assaf, C. Alvarez, M. Bertoglio, R. Clérac, K. Hoummada, C. Alfonso, A. Charai, O. Pilone, K. Hahn, V. Dolocan, S. Bertaina, Ferromagnetic MnCoGe thin films produced via magnetron sputtering and non-diffusive reaction, Appl. Surf. Sci. 437 (2018) 336–346.
[34] D.B. Cuttris, Relation Between Surface Concentration and Average Conductivity in Diffused Layers in Germanium, Bell Syst. Techn. J 40 (1961) 509–521.

[35] B. Poudel, Q. Hao, Y. Ma, Y. Lan, A. Minnich, B. Yu, X. Yan, D. Wang, A. Muto, D. Vashaee, X. Chen, J. Liu, M.S. Dresselhaus, G. Chen, Z. Ren, High-Thermoelectric Performance of Nanostructured Bismuth Antimony Telluride Bulk Alloys, Science 320 (2008) 634–638.

[36] L.-.D. Zhao, G. Tan, S. Hao, J. He, Y. Pei, H. Chi, H. Wang, S. Gong, H. Xu, V.P. Dravid, C. Uher, G.J. Snyder, C. Wolverton, M.G. Kanatzidis, Ultrahigh power factor and thermoelectric performance in hole-doped single-crystal SnSe, Science 351 (2016) 141–144.

[37] W. He, D. Wang, H. Wu, Y. Xiao, Y. Zhang, D. He, Y. Feng, Y.-.J. Hao, J.-.F. Dong, R. Chetty, L. Hao, D. Chen, J. Qin, Q. Yang, X. Li, J.-.M. Song, Y. Zhu, W. Xu, C. Niu, µ.X. Li, G. Wang, C. Liu, M. Ohta, S.J. Pennycook, J. He, J.-.F. Li, L.-.D. Zhao, High thermoelectric performance in low-cost $SnS_{0.91}Se_{0.09}$ crystals, Science 365 (2019) 1418–1424.

[38] W. Liu, H.S. Kim, S. Chen, Q. Jie, B. Lv, M. Yao, Z. Ren, C.P. Opeil, S. Wilson, C.-.W. Chu, Z. Ren, n-type thermoelectric material $Mg_2Sn_{0.75}Ge_{0.25}$ for high power generation, Proc. Nat. Ac. Sci 112 (2015) 3269–3274.

[39] Sheng S. Li, Transport Properties of Semiconductors, in: Semiconductor Physical Electronics, Springer, New York, 2007, pp. 171–210.

[40] V. Vargiamidis, M. Thesberg, N. Neophytou, Theoretical model for the Seebeck coefficient in superlattice materials with energy relaxation, J. Appl. Phys 126 (2019) 055105.

[41] H.J. Goldsmid, J.W. Sharp, Estimation of the thermal band gap of a semiconductor from seebeck measurements, J. Elec. Mat 28 (1999) 869–872.

[42] S. Gupta, B. Magyari-Köpe, Y. Nishi, K.C. Saraswat, Achieving direct band gap in germanium through integration of Sn alloying and external strain, J. Appl. Phys 113 (2013) 073707.

[43] M.P. Polak, P. Scharoch, R. Kudrawiec, The electronic band structure of $Ge_{1-x}Sn_x$ in the full composition range: indirect, direct, and inverted gaps regimes, band offsets, and the Burstein–Moss effect, J. Phys. D: Appl. Phys 50 (2017) 195103.

[44] S. Zaima, O. Nakatsuka, Y. Shimura, M. Adachi, M. Nakamura, S. Takeuchi, B. Vincent, F. Gencarelli, T. Clarysse, J. Demeulemeester, K. Temst, A. Vantomme, M. Caymax, R. Loo, (Invited) GeSn Technology: Impact of Sn on Ge CMOS Applications, ECS Trans 41 (2011) 231.

[45] E. Kamiyama, S. Nakagawa, K. Sueoka, T. Ohmura, T. Asano, O. Nakatsuka, N. Taoka, S. Zaima, K. Izunome, K. Kashima, Effect of Sn atoms on incorporation of vacancies in epitaxial $Ge_{1-x}Sn_x$ film grown at low temperature, Appl. Phys. Exp 7 (2014) 021302.

[46] W. Takeuchi, T. Asano, Y. Inuzuka, M. Sakashita, O. Nakatsuka, S. Zaima, Characterization of Shallow- and Deep-Level Defects in Undoped $Ge_{1-x}Sn_x$ Epitaxial Layers by Electrical Measurements, ECS J. Sol. State Sci. Tech. 5 (2016) P3082.

[47] A. Chroneos, Isovalent impurity-vacancy complexes in germanium, Phys. Status Solidi B 244 (2007) 3206–3210.

[48] T. Ueno, T. Irisawa, Y. Shiraki, A. Uedono, S. Tanigawa, Low temperature buffer growth for modulation doped SiGe/Ge/SiGe heterostructures with high hole mobility, Thin Solid Films 369 (2000) 320–323.

[49] A.P. Knights, R.M. Gwilliam, B.J. Sealy, T.J. Grasby, C.P. Parry, D.J.F. Fulgoni, P.J. Phillips, T.E. Whall, E.H.C. Parker, P.G. Coleman, Growth temperature dependence for the formation of vacancy clusters in $Si/Si_{0.64}Ge_{0.36}/Si$ structures, Appl. Phys. Lett 89 (2001) 76–79.

[50] K. Moto, N. Saitoh, N. Yoshizawa, T. Suemasu, K. Toko, Solid-phase crystallization of densified amorphous GeSn leading to high hole mobility ($540\,cm^2/Vs$), Appl. Phys. Lett. 114 (2019) 112110.

[51] N. Neophytou, X. Zianni, H. Kosina, S. Frabboni, B. Lorenzi, D. Narducci, Simultaneous increase in electrical conductivity and Seebeck coefficient in highly boron-doped nanocrystalline Si, Nano 24 (2013) 205402.

[52] J. Nicolas, S. Assali, S. Mukherjee, A. Lotnyk, O. Moutanabbir, Dislocation Pipe Diffusion and Solute Segregation during the Growth of Metastable GeSn, Cryst. Growth Des 20 (2020) 3493–3498.

[53] R. Roucka, R. Beeler, J. Mathews, M.-.Y. Ryu, Y.K. Yeo, J. Menéndez, J. Kouvetakis, Complementary metal-oxide semiconductor-compatible detector materials with enhanced 1550 nm responsivity via Sn-doping of Ge/Si(100), J. Appl. Phys. 109 (2011) 103115.

[54] J. Xie, J. Tolle, V.R. D'Costa, C. Weng, A.V.G. Chizmeshya, J. Menendez, J. Kouvetakis, Molecular approaches to p- and n-nanoscale doping of $Ge_{1-y}Sn_y$ semiconductors: Structural, electrical and transport properties, Solid State Electron 53 (2009) 816–823.

[55] V.R. D'Costa, C.S. Cook, A.G. Birdwell, C.L. Littler, M. Canonico, S. Zollner, J. Kouvetakis, J. Menéndez, Optical critical points of thin-film Ge_{1-y} Sn_y alloys: A comparative Ge_{1-y} Sn_y Ge_{1-x} six study, Phys. Rev. B 73 (2006) 125207.

[56] K.R. Khiangte, J.S. Rathore, J. Schmidt, H.J. Osten, A. Laha, S. Mahapatra, Wafer-scale all-epitaxial GeSn-on-insulator on Si(111) by molecular beam epitaxy, J. Phys. D: Appl. Phys 51 (2018) 32LT01.

[57] S. Prucnal, Y. Berencén, M. Wang, L. Rebohle, R. Böttger, I.A. Fischer, L. Augel, M. Oehme, J. Schulze, M. Voelskow, M. Helm, W. Skorupa, S. Zhou, Ex situ n^+ doping of GeSn alloys via non-equilibrium processing, Semicond. Sci. Technol 33 (2018) 065008.

[58] C. Schulte-Braucks, Investigation of GeSn as Novel Group IV Semiconductor for Electronic Applications, Schlüsseltechnologien Key Technologies Band, 168, Forschungszentrum Jülich, 2018 ISBN 978-3-95806-312-92017.

[59] N. Uchida, J. Hattori, R.R. Lieten, Y. Ohshi, R. Takase, M. Ishimaru, K. Fukuda, T. Maeda, J.-.P. Locquet, Carrier and heat transport properties of poly-crystalline GeSn films for thin-film transistor applications, J. Appl. Phys 126 (2019) 145105.